Biomedical Physics & Engineering Express

PAPER

Differentiation between normal and tumor mammary glands with depth-resolved attenuation coefficient from optical coherence tomography

RECEIVED
27 July 2021

REVISED
12 October 2021

ACCEPTED FOR PUBLICATION
9 November 2021

PUBLISHED
18 November 2021

Marino J Maciel[1,*], Hugo M Pereira[1,*], Sara Pimenta[1], Alice Miranda[2], Eduardo J Nunes-Pereira[3] and José H Correia[1]

[1] CMEMS-UMinho, University of Minho, Guimarães, Portugal
[2] ICVS, School of Medicine, University of Minho, ICVS/3B's - PT Government Associate Laboratory, Braga/Guimarães, Portugal
[3] Centre of Physics of Minho and Porto Universities (CF-UM-UP), University of Minho, Braga, Portugal
[*] Authors to whom any correspondence should be addressed.

E-mail: mmaciel@dei.uminho.pt **and** hugo.pereira@dei.uminho.pt

Keywords: OCT imaging, attenuation coefficient, mammary mouse glands

Abstract

Optical coherence tomography (OCT) is a well-established imaging technology for high-resolution, cross-sectional imaging of biological tissues. Imaging processing and light attenuation coefficient estimation allows to further improve the OCT diagnostic capability. In this paper we use a commercial OCT system, Telesto II-1325LR from Thorlabs, and demonstrate its ability to differentiate normal and tumor mammary mouse glands with the OCT attenuation coefficient. Using several OCT images of normal and tumor mammary mouse glands (n = 26), a statistical analysis was performed. The attenuation coefficient was calculated in depth, considering a slope of 0.5 mm. The normal glands present a median attenuation coefficient of 0.403 mm^{-1}, comparatively to 0.561 mm^{-1} obtained for tumor mammary glands. This translates in an attenuation coefficient approximately 39% higher for tumor mammary glands when compared to normal mammary glands. The OCT attenuation coefficient estimation eliminates the subjective analysis provided by direct visualization of the OCT images.

1. Introduction

Optical coherence tomography (OCT) is a high-resolution imaging technology, which allows to obtain depth-resolved images of biological tissues by optical interferometrical measurement [1, 2]. OCT is the parallel of the ultrasound B-scan technology, using light instead of sound waves. In ultrasonography, an image is formed by registering the detected echoes of the emitted sound waves: the time delay between sound emission and echo detection provides depth information, while its magnitude provides B-(Brightness) information [3, 4]. OCT uses a low-coherence interferometry (the backscattered light is interfered with the emitted light beam) and a near-infrared optical source. Depending on the bandwidth and central wavelength of the optical source, the current OCT technologies have an axial resolution range from 1 to 15 μm, 10–100 times finer than the standard ultrasound imaging systems. The OCT depth imaging of regular commercial systems is approximately 2 mm, but this parameter is limited by the optical source and light scattering in biological tissues [1, 5–7]. OCT started as a promising and powerful tool in ophthalmology [8], however, in the last decade, OCT has also been applied to other fields of medicine, due to its sub-micrometer resolution and real-time imaging possibility [5, 9].

The use of optical systems for clinical imaging of pathological conditions, such as precancer/cancer diagnosis, is today, more than ever, an important and emergent topic of investigation in biomedical research. The optical properties of different tissues result in different imaging characteristics, providing morphological and physiological information about them. In particular, it is very important to obtain the inner structure characteristics of the tissues for precancer detection and OCT plays an important role in this field, as it provides cross-sectional imaging of the tissue microstructure with high axial resolution [10, 11].

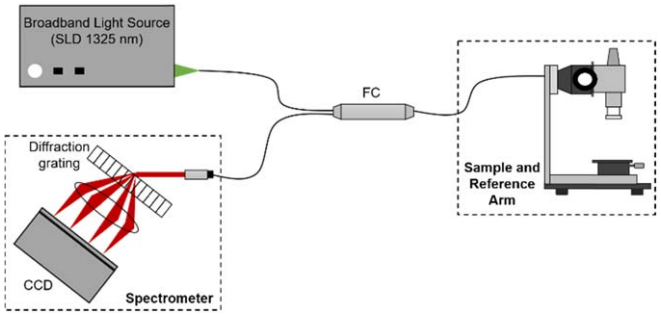

Figure 1. Schematic of the SD-OCT system Telesto II-1325 LR, from Thorlabs. Reproduced with permission from [26] Thorlabs, Inc.

The intensity of the coherent light propagating through a biological medium is attenuated along its depth due to light absorption and scattering phenomena. This attenuation is described by the Beer–Lambert law, and its magnitude as a function of the depth is characterized by the attenuation coefficient. The attenuation of light depends on the specific optical properties of the medium, which means that determining the attenuation coefficient provides valuable information about the biological tissues being analyzed [12–14]. Several studies have demonstrated the potential of the quantitative OCT analysis for diagnosis and classification purposes: renal [15], oral [16], liver [17] and rectal [18] cancer diagnosis, skin lesions [19], bladder cancer tumor staging [20], glaucoma diagnosis [21], malignant axillary lymph node diagnosis [12], brain cancer infiltration [22]/tumorous human brain quantitative diagnosis [23], and atherosclerotic plaque characterization [24]. OCT imaging was also used to study supercontinuum laser-induced cutaneous thermal injuries and consequent repair in living mice, by qualitative and quantitative evaluation [25]. To the authors' current knowledge, this is the first report about the differentiation of normal and tumor mammary glands by analyzing the attenuation coefficient of OCT images.

In this paper, we introduce a method to differentiate between normal and tumor mammary glands provided by OCT images, based on the estimation of the attenuation coefficient of light along the depth of the tissue. A brief introduction of the OCT technology in biological tissues examination and the importance of the quantitative analysis provided by the attenuation coefficient is described in this section. Section 2 presents the methods used for OCT imaging acquisition and for the attenuation coefficient estimation. The process for image noise reduction, and the statistical analysis method is also described. The results for normal and tumor mammary glands are presented and discussed in section 3, including: OCT images, OCT attenuation coefficient calculation and the statistical analysis. Finally, the conclusion of this study is presented in section 4.

2. Methods

2.1. OCT imaging of biological tissues

OCT can be implemented in two ways: time and frequency domain. The introduction of frequency domain (FD-OCT) systems increased the speed of imaging acquisition. FD-OCT does not require the movement of a reference mirror, as required in time domain OCT, and measures the full depth of the sample simultaneously. The FD-OCT systems can be implemented in two ways: by using a broadband optical source and a spectrometer, spectral domain OCT (SD-OCT), or by using a swept source and a photodiode, swept-source OCT (SS-OCT). The performance of an OCT system is influenced by the optical source, and the choice of the spectral range depends on the intended application. In retinal imaging it is common to use either 800 nm (higher resolution) or 1000 nm (higher penetration depth). To obtain OCT images of deeper structures it is required to use light at higher wavelengths, due to the decreased scattering properties. In this study, a SD-OCT system Telesto II-1325 LR, from Thorlabs, was used. The system uses a superluminescent diode (SLD) centered at 1325 nm and presents a theoretical axial resolution of 12 μm/9 μm and an imaging depth of 7.0 mm/5.3 mm (air/water). Lateral resolution of the OCT system is decoupled from the axial resolution: while the axial resolution is controlled by the spectral bandwidth of SLD, the lateral resolution is controlled by optics. The imaging probe of Telesto II contains a Michelson-type interferometer, two galvanometric scanning mirrors and a telecentric scanning objective (OCT-LK4 optical kit from Thorlabs, which provides a lateral resolution of 20 μm). The spectrometer specifications fix a pixel size vertical resolution of 6.91 μm. Figure 1 presents a schematic of the Telesto II-1325 LR system, used for OCT imaging acquisition.

OCT images were collected from resected mammary glands of a mouse. Normal and tumor mammary glands were used in this study. The tissues derived from an animal that was maintained in approved rodent facilities and all the personnel involved in experimental procedures with animals are

approved by the national competent authority (Direcção Geral de Alimentação e Veterinária - DGAV). The tissues were collected from a mouse that, although being included in approved experimental projects by the institutional animal welfare body (ORBEA) and by DGAV, has spontaneously developed mammary tumors and humane endpoints were applied in due time. This means that the animal was not submitted to tumor induction or other existing experimental procedures to introduce the tumors. The use of animal tissues derived from animals that develop spontaneous diseases contribute to the 3Rs of Russell and Burch: wherever possible, the use of animals should be replaced, refined, and reduced. This study contributes to the aforementioned 3Rs in a way that animal numbers for scientific research purposes can be significantly reduced.

The ultimate objective of this study is to differentiate the two types of glands, normal and tumor, basing on the OCT imaging technique and consequent attenuation coefficient (μ_{OCT}) estimation. The B-scans of the normal and tumor mammary glands were acquired with a field of view (FOV) of 4.5 × 4.0 mm (lateral and axial/depth direction).

2.2. Estimation of the attenuation coefficient

The model of light-tissue interaction is based on the differential equation for attenuation of the coherent light beam, according to the Lambert-Beer's law—equation (1).

$$dL(z) = -\mu(z)L(z)dz \tag{1}$$

where μ(z) is the depth-dependent attenuation coefficient, expressed in mm^{-1}, z is the depth in mm, and L(z) is the irradiance of the incident light beam, expressed in Wm^{-2}. The Lambert-Beer's equation provides a linear relationship between the amount of the attenuated irradiance and the irradiance of the incident light. L(z) can be expressed in relation to the boundary condition $L(0) = L_0$, the irradiance of the incident beam.

$$L(z) = L_0 e^{-\int_0^z \mu(u)du} \tag{2}$$

The back scattered irradiance ($Wm^{-2}mm^{-1}$) detected and converted into a digital signal in the OCT detecting system is expressed according to the equation (3),

$$I(z) = \alpha\beta\mu(z)L_0 e^{-2\int_0^z \mu(u)du}, \tag{3}$$

where I(z) is the back scattered irradiance, α is a fixed fraction of the attenuated light that is back scattered, and β is a conversion factor that counts for the digitization and integration of the signal, according to the size of detector and axial sampling density [13].

In order to estimate the definite integral I(z), the boundary condition is applied $I(\infty) = 0$, and the following equation is obtained:

$$\int_z^\infty I(u)du = -\frac{I(u)}{2\mu(u)} + c\Big|_z^\infty = \frac{I(z)}{2\mu(z)} \tag{4}$$

Solving the equation (4) for the attenuation coefficient and taking into account the limited depth range D of the OCT system, the equation (5) is obtained.

$$\mu_{OCT}(z) = \frac{I(z)}{2\int_z^\infty I(u)du} \approx \frac{I(z)}{2\int_z^D I(u)du} \tag{5}$$

The equation (5) is defined on a continuous domain, but OCT system only provides discretized measurements. The OCT signal I[i] is given by the integrated signal over a small distance, defined by the pixel size Δ, which is commonly related to the coherence length of the OCT light source. The equation (6) was used to estimate the depth-resolved attenuation coefficient of the OCT signal (μ_{OCT}).

$$\mu_{OCT}[i] \approx \frac{I[i]}{2\Delta\sum_{i+1}^{\infty} I[i]} \tag{6}$$

2.3. Image acquisition and statistical analysis

For each OCT acquisition, each B-scan image analyzed was a result of an average of 10 frames scanned over roughly 1 s. Each B-scan image had a resolution of 4500 × 579 pixels (lateral and axial/depth direction), with an axial pixel size of 6.91 μm, corresponding to a FOV of 4.5 × 4.0 mm. Before calculation of the attenuation coefficient, a noise image, with the same aforementioned resolution, was subtracted to each OCT image of the biological tissue in order to minimize the influence of equipment-related noise. The noise image was obtained by using the OCT system Telesto II without any sample in the sample arm of the interferometer. A central region of 1.25 mm (in the lateral direction) of the resulting B-scan has been selected to depth-calculate the attenuation coefficient in 13 normal and 13 tumor tissue images (13 × 1250 A-scans for each type of tissue). Since it is a pixel-by-pixel calculation, each of the selected A-scans was transformed into a depth-resolved attenuation coefficient curve, according to equation (6). A slope of 0.5 mm starting at the air/tissue interface was then used to calculate the resulting attenuation coefficients average for each A-scan.

3. Results and discussion

Figures 2(a) and 3(a) present 3D OCT images of normal and tumor mammary glands, respectively. These images are merely representative and were not used for the estimation of the attenuation coefficient. Figures 2(b) and 3(b) represent a 2D OCT image of normal and tumor mammary glands, respectively, resulting from the average of 10 B-scans with consequent noise elimination. The OCT images from the normal and tumor mammary glands are notably different. In the OCT image of normal mammary glands (figure 2), it is

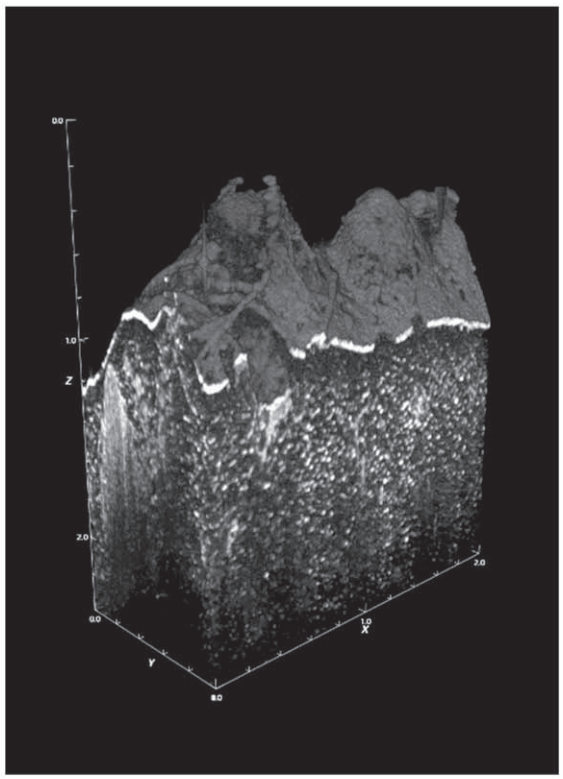

Figure 2. OCT images of resected normal mammary glands of a mouse: (a) 3D OCT volume, with (x, y, z) (2.0; 1.0; 2.49) mm dimension and (b) B-scan without noise.

possible to see a separation of different layers within the tissue with depth increase. In contrast, the OCT image of the tumor mammary glands (figure 3) does not present a clear difference in tissue morphology with increased depth, exhibiting a high degree of homogeneity and a lack of layer differentiation.

For each OCT image, a 1.25 mm lateral region-of-interest (1250 A-scans) was selected to calculate the light attenuation coefficient in depth, according to equation (6). The pixel size of the acquired images is 6.91 μm. Figures 4 and 5 present two random A-scans of the normal and tumor mammary glands, respectively, with the correspondent attenuation coefficient curve expressed in mm^{-1}.

The statistical analysis performed is based on the attenuation coefficient curve calculated for each

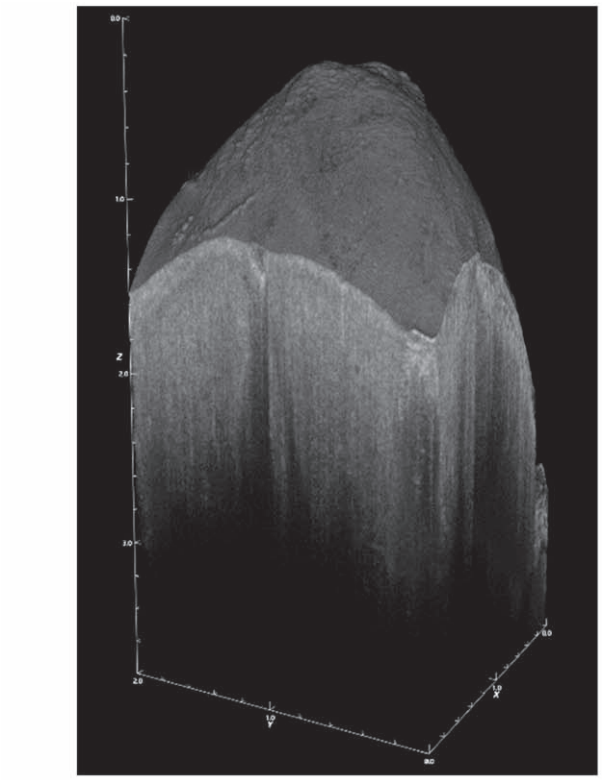

(a)

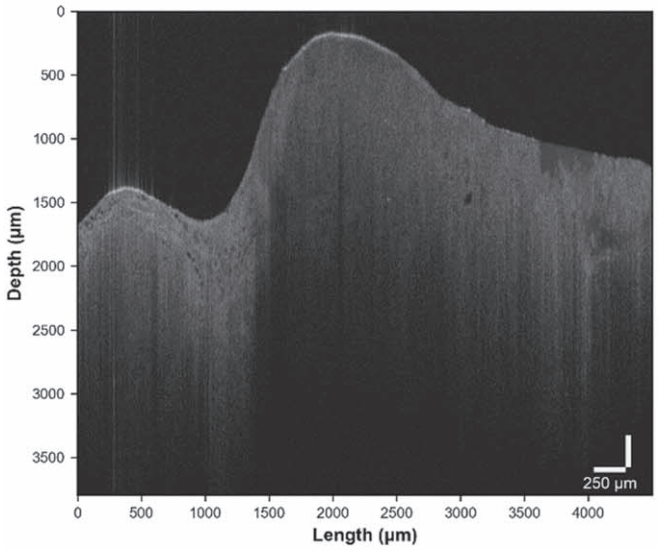

(b)

Figure 3. OCT images of resected tumor mammary glands of a mouse: (a) 3D OCT volume, with (x, y, z) (2.0; 2.0; 4.0) mm dimension and (b) B-scan without noise.

A-scan obtained. A slope of 0.5 mm in depth in the attenuation coefficient curve was automatically selected, by means of edge detection algorithms, to calculate the average of the attenuation coefficient values at the immediate interface between air and tissue. This results in 1250 OCT attenuation coefficients per B-scan image (13 × 1250 for each type of tissue).

Figure 6 presents the mean of the attenuation coefficient for each tissue (n = 26). The standard deviation error is also depicted. Figure 7 plots the mean of the attenuation coefficient for each sample of tumor and normal mammary glands. In this graphic, it is possible to conclude that the OCT attenuation coefficients are significantly higher for tumor tissues than for normal tissues for the mammary glands analyzed.

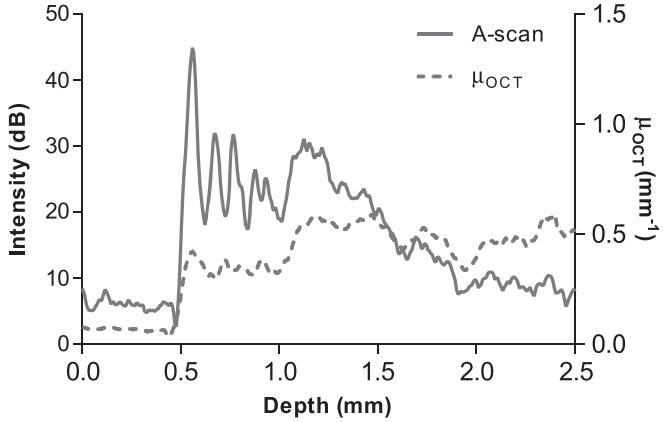

Figure 4. A random depth profile (A-scan) and the correspondent attenuation coefficient curve obtained from an OCT image of resected normal mammary gland of a mouse.

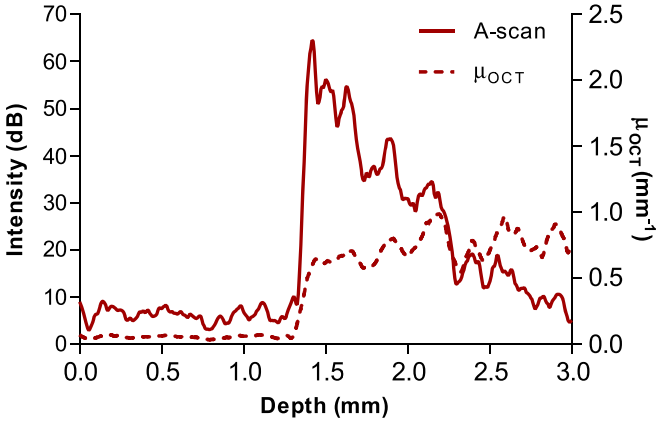

Figure 5. A random depth profile (A-scan) and the correspondent attenuation coefficient curve obtained from an OCT image of resected tumor mammary gland of a mouse.

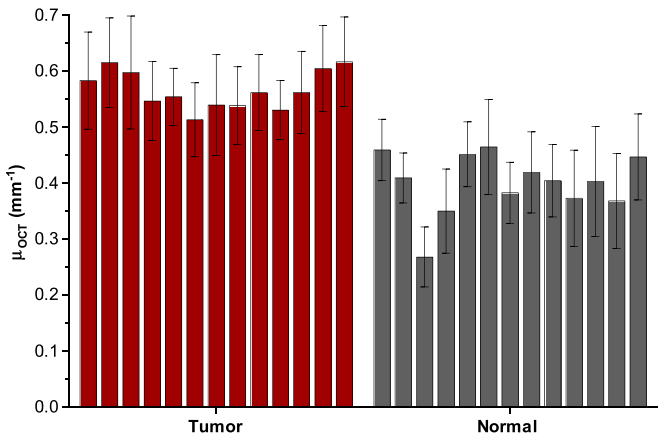

Figure 6. Attenuation coefficients of resected tumor and normal mammary glands of a mouse, n = 26.

Table 1 summarizes the main results obtained for this study. The mean OCT attenuation coefficient of normal tissue ($0.401 \pm 0.0885\ mm^{-1}$) is lower than that of the tumor tissue ($0.567 \pm 0.0826\ mm^{-1}$). The median OCT attenuation coefficient of each tissue is also presented in table 1 and depicted in the boxplot of figure 8. Again, the median of the normal mammary glands ($0.403\ mm^{-1}$) is lower than that obtained for the tumor mammary glands ($0.561\ mm^{-1}$).

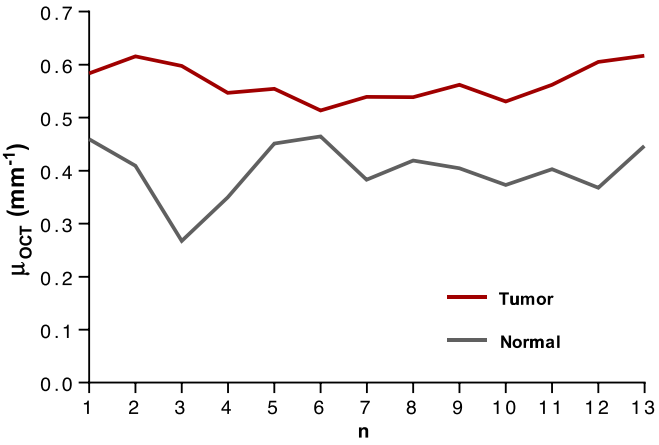

Figure 7. Attenuation coefficient difference between tumor and normal mammary glands of a mouse.

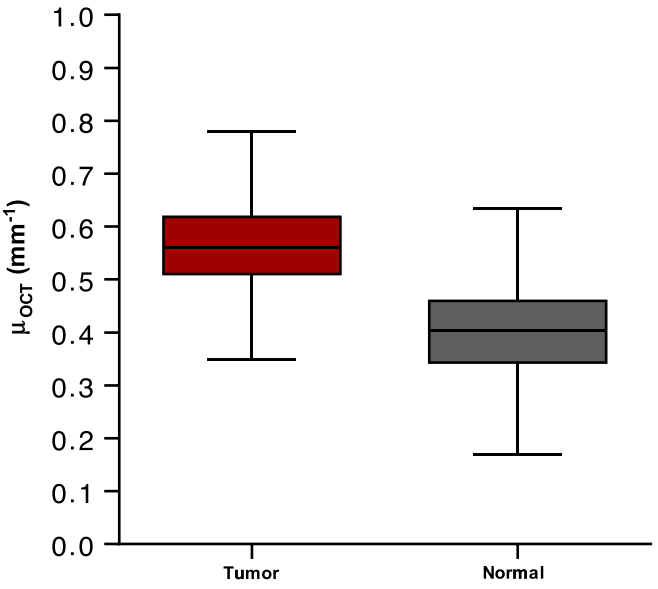

Figure 8. Boxplot showing the median OCT attenuation coefficient of the tumor and normal mammary glands.

Table 1. Mean, standard deviation (SD) and median of the statistical analysis towards OCT attenuation coefficient of resected normal and tumor mammary glands of a mouse.

Mammary glands	Normal (n = 13)	Tumor (n = 13)
Mean (mm^{-1})	0.401	0.567
SD (mm^{-1})	0.0885	0.0826
Median (mm^{-1})	0.403	0.561

4. Conclusion

In this study we report the results of OCT performed in resected normal and tumor mammary glands of a mouse. The results proved the potential of the OCT imaging in the differentiation of normal and tumor tissues. The *ex-vivo* OCT imaging of normal mammary mouse glands showed a clear separation of the tissue layers in depth. In contrast, this separation was not evident in the OCT image of the tumor mammary gland. A quantitative analysis of the OCT images was performed considering the attenuation coefficient, based on a depth-resolved algorithm. Using a 0.5 mm slope in the depth profile of OCT images, the obtained attenuation coefficient for tumor mammary glands (mean of 0.567 mm^{-1} and median of 0.561 mm^{-1}) is higher than that obtained for the normal tissues (mean of 0.401 mm^{-1} and median of 0.403 mm^{-1}). The statistical analysis in 26 OCT images of normal and tumor tissues, considering a lateral length of 1.25 mm (1250 A-scans), proves a quantitative differentiation between the two tissues.

In conclusion, OCT provides a high-resolution and in-depth cross-sectional images of biological tissues, suitable for quantitative analysis. With this study we present the potential of the attenuation coefficient to provide a quantitative analysis of resected mammary glands of a mouse, where the OCT attenuation

coefficient of tumor tissues is higher than normal tissues, proving to be an important parameter in distinguishing different types of tissues.

Acknowledgments

This work is supported by:-OCT-RAMAN, PTDC/FIS-OTI/28296/2017 with the operation code NORTE-01-0145-FEDER-028296;—MPhotonBiopsy, PTDC/FIS-OTI/1259/2020;—CMEMS-UMinho Strategic Project UIDB/04436/2020;- Infrastructures Micro&Nano-Fabs@PT, operation code NORTE 01-0145-FEDER-022090, POR Norte, Portugal.

Data availability statement

All data that support the findings of this study are included within the article (and any supplementary files).

ORCID iDs

Marino J Maciel https://orcid.org/0000-0002-1752-2687
Hugo M Pereira https://orcid.org/0000-0003-4093-103X
Sara Pimenta https://orcid.org/0000-0002-6061-320X
Alice Miranda https://orcid.org/0000-0002-7297-9639
Eduardo J Nunes-Pereira https://orcid.org/0000-0002-3654-4363
José H Correia https://orcid.org/0000-0001-5991-1069

References

[1] Drexler W and Fujimoto J G 2015 *Optical Coherence Tomography: Technology and Applications ed Springer* (Switzerland: Springer International Publishing)
[2] Adler D C, Zhou C, Tsai T-H, Schmitt J, Huang Q, Mashimo H and Fujimoto J G 2009 Three-dimensional endomicroscopy of the human colon using optical coherence tomography *Opt. Express* **17** 784–96
[3] Familiari L *et al* 2006 Optical coherence tomography evaluation of ulcerative colitis: the patterns and the comparison with histology *Am. J. Gastroenterol.* **101** 2833–40
[4] Valery V T 2014 *Tissue Optics: Light Scattering Methods And Instruments For Medical Diagnosis* (Bellingham, WA: SPIE)
[5] Maciel M J, Rosa C C, Wolffenbuttel R F and Correia J H 2018 Optical coherence tomography within a single microsystem *J. Phys. D. Appl. Phys.* **51** 365401
[6] Aguirre A D, Chen Y, Bryan B, Mashimo H, Huang Q, Connolly J L and Fujimoto J G 2010 Cellular resolution *ex vivo* imaging of gastrointestinal tissues with optical coherence microscopy *J. Biomed. Opt.* **15** 016025
[7] Balas C 2009 Review of biomedical optical imaging—a powerful, non-invasive, non-ionizing technology for improving *in vivo* diagnosis *Meas. Sci. Technol.* **20** 104020
[8] Huang D *et al* 1991 Optical coherence tomography *Science* **254** 1178–81
[9] Ling C H-Y, Pozzi A, Thieman K M, Tonks C A, Guo S, Xie H and Horodyski M 2010 The potential of optical coherence tomography for diagnosing meniscal pathology *Meas. Sci. Technol.* **21** 045801
[10] Chen Y *et al* 2007 Ultrahigh resolution optical coherence tomography of Barrett's esophagus: preliminary descriptive clinical study correlating images with histology *Endosc. 2007* **39** 599–605
[11] Zhao Q, Wei H, He Y, Ren Q and Zhou C 2014 Evaluation of ultrasound and glucose synergy effect on the optical clearing and light penetration for human colon tissue using SD-OCT *J. Biophotonics* **7** 938–47
[12] McLaughlin R A, Scolaro L, Robbins P, Saunders C, Jacques S L and Sampson D D 2010 Parametric imaging of cancer with optical coherence tomography *J. Biomed. Opt.* **15** 046029
[13] Vermeer K A, Mo J, Weda J J A, Lemij H G and de Boer J F 2014 Depth-resolved model-based reconstruction of attenuation coefficients in optical coherence tomography *Biomed. Opt. Express* **5** 322
[14] Smith G T, Dwork N, O'Connor D, Sikora U, Lurie K L, Pauly J M and Ellerbee A K 2015 Automated, depth-resolved estimation of the attenuation coefficient from optical coherence tomography data *IEEE Trans. Med. Imaging* **34** 2592–602
[15] Barwari K, de Bruin D M, Faber D J, van Leeuwen T G, de la Rosette J J and Laguna M P 2012 Differentiation between normal renal tissue and renal tumours using functional optical coherence tomography: a phase I *in vivo* human study *BJU Int.* **110** E415–20
[16] Tomlins P H, Adegun O, Hagi-Pavli E, Piper K, Bader D and Fortune F 2010 Scattering attenuation microscopy of oral epithelial dysplasia *J. Biomed. Opt.* **15** 066003
[17] Zhou F, Wei H, Ye X, Hu K, Wu G, Yang H, He Y, Xie S and Guo Z 2015 Influence of nanoparticles accumulation on optical properties of human normal andcancerous liver tissue *in vitro* estimated by OCT *Phys. Med. Biol.* **60** 1385–97
[18] Zhang Q Q, Wu X J, Tang T, Zhu S W, Yao Q, Gao B Z and Yuan X C 2012 Quantitative analysis of rectal cancer by spectral domain optical coherence tomography *Phys. Med. Biol.* **57** 5235–44
[19] Liu Z, Guo Z, Zhuang Z, Zhai J, Xiong H and Zeng C 2010 Quantitative optical coherence tomography of skin lesions induced by different ultraviolet B sources *Phys. Med. Biol.* **55** 6175–85
[20] Cauberg E C C, de Bruin D M, Faber D J, de Reijke T M, Visser M, de la Rosette J J M C H and van Leeuwen T G 2010 Quantitative measurement of attenuation coefficients of bladder biopsies using optical coherence tomography for grading urothelial carcinoma of the bladder *J. Biomed. Opt.* **15** 066013
[21] van der Schoot J, Vermeer K A, de Boer J F and Lemij H G 2012 The effect of glaucoma on the optical attenuation coefficient of the retinal nerve fiber layer in Spectral Domain Optical Coherence Tomography images *Investig. Ophthalmol. Vis. Sci.* **53** 2424–30
[22] Kut C, Chaichana K L, Xi J, Raza S M, Ye X, McVeigh E R, Rodriguez F J, Quiñones-Hinojosa A and Li X 2015 Detection of human brain cancer infiltration *ex vivo* and *in vivo* using quantitative optical coherence tomography *Sci. Transl. Med.* **7** 292ra100–92ra100
[23] Yashin K S *et al* 2019 Quantitative nontumorous and tumorous human brain tissue assessment using microstructural co- and cross-polarized optical coherence tomography *Sci. Rep.* **9** 2024
[24] van Soest G *et al* 2010 Atherosclerotic tissue characterization in vivo by optical coherence tomography attenuation imaging *J. Biomed. Opt.* **15** 011105
[25] Fan Y, Ma Q, Xin S, Peng R and Kang H 2021 Quantitative and qualitative evaluation of supercontinuum laser-induced cutaneous thermal injuries and their repair with OCT images *Lasers Surg. Med.* **53** 252–62
[26] Thorlabs 2021 Telesto® series SD-OCT systems *OCT Tutor* (https://www.thorlabs.com/newgrouppage9.cfm?objectgroup_id=12569&pn=TEL220C1)